See this record in the RMIT Research Repository at:

https://researchbank.rmit.edu.au/view/rmit:34276

Version: Accepted Manuscript

Copyright Statement:

Link to Published Version:

https://dx.doi.org/10.1038/nphoton.2013.287

Ultra-Large-Scale Continuous-Variable Cluster States Multiplexed in the Time Domain

Shota Yokoyama[1], Ryuji Ukai[1], Seiji C. Armstrong[1,2],
Chanond Sornphiphatphong[1], Toshiyuki Kaji[1], Shigenari Suzuki[1],
Jun-ichi Yoshikawa[1], Hidehiro Yonezawa[1],
Nicolas C. Menicucci[3], Akira Furusawa[1]*

[1]Department of Applied Physics, School of Engineering, The University of Tokyo,
7-3-1 Hongo, Bunkyo-ku, Tokyo 113-8656, Japan
[2]Centre for Quantum Computation and Communication Technology,
Department of Quantum Science, The Australian National University,
Canberra, ACT 0200, Australia
[3]School of Physics, The University of Sydney, NSW, 2006, Australia

*To whom correspondence should be addressed; E-mail: akiraf@ap.t.u-tokyo.ac.jp

Quantum computers promise ultrafast performance of certain tasks[1]. Experimentally appealing, measurement-based quantum computation (MBQC)[2] requires an entangled resource called a cluster state[3], with long computations requiring large cluster states. Previously, the largest cluster state consisted of 8 photonic qubits[4] or light modes[5], while the largest multipartite entangled state of any sort involved 14 trapped ions[6]. These implementations involve quantum entities separated in space, and in general, each experimental apparatus is used only once. Here, we circumvent this inherent inefficiency by multiplexing light modes in the time domain. We deterministically generate and fully characterise a continuous-variable cluster state[7,8] containing more than 10,000 entangled modes. This is, by 3 orders of magnitude, the largest entangled state ever created to date. The entangled modes are individually addressable wavepackets of light in two beams. Furthermore, we present an efficient scheme for MBQC on this cluster state based on sequential applications of quantum teleportation.

Originally formulated as a demonstration as to why quantum mechanics must be incomplete in the famous 1935 Einstein-Podolsky-Rosen (EPR) paradox[9], entanglement is now recognized as a signature feature of quantum physics[10], and it plays a central role in various quantum information processing (QIP) protocols[1,11]. For example, the bipartite entangled state known as an EPR state[9] is a resource for quantum teleportation (QT), whereby a quantum state is transferred from one location to another without physical transfer of the quantum information[12–14].

Measurement-based quantum computation (MBQC)[2,7,8,15–18], which is based on the QT of information and logic gates, requires the special class of multipartite entangled resource states known as cluster states[3]. The number of entangled quantum entities and their entanglement structure (represented by a graph) determines the resource space available for computation. Ultra-large-scale QIP (which could be based on MBQC) will require ultra-large-scale entangled

2

states[2,7,8].

In the vast majority of optical experiments, quantum modes are distinguished from each other by their spatial location. This leads to an inherent lack of scalability as each additional entangled party requires an increase in laboratory equipment and dramatically increases the complexity of the optical network[19,20]. Further, due to the probabilistic nature of photon pair generation, demonstrations involving the postselection of photonic qubits[4,15,16] suffer from dramatically reduced event success rates with each additional qubit.

One method to overcome this problem of scalability is to deterministically encode the modes within one beam. Entanglement between quadrature-phase amplitudes in continuous-wave laser beams has been deterministically created and exploited in QIP[5,13,14,17–19,21–23], even though the quantum correlations are finite. Previous attempts to deterministically create cluster states within one beam have exploited the spatial[21] or spectral[22–24] orthogonality of quantum modes. While such methods are potentially scalable, current experimental results are limited to generating entangled states of just a few modes each[21–23]. A novel method proposed in ref. 25 lets quantum modes propagate within the same beam — distinguished and ultimately made orthogonal by their separation in time. The time-domain multiplexing approach allows each additional quantum mode to be manipulated by the same optical components at different times, which is a powerful concept, as found in atomic ensemble quantum memories[26].

Here, we demonstrate the deterministic generation of ultra-large-scale entangled states consisting of more than $10,000$ entangled wave-packets of light, multiplexed in the time domain. The generated states, which we call extended EPR (XEPR) states, are equivalent up to local phase shifts to topologically one-dimensional continuous-variable (CV) cluster states[25] and are therefore a universal resource for single-mode MBQC with continuous-variables[8]. Fully universal multimode MBQC is achievable simply by combining two XEPR states with differing time delays on two additional beam-splitters[25]. Note that in our time-domain multiplexed demonstra-

3

tion only a small part of the entire XEPR state exists at each instant of time. This is the reason why we could achieve such an efficient setup for the creation and verification of an ultra-large number of entangled modes.

The XEPR states are generated by entangling together sequentially propagating EPR states contained within two beams. This can be viewed as four distinct steps, as illustrated in Fig. 1a. First, two continuous-wave squeezed light beams are generated from two optical parametric oscillators (OPOs) (Step i). We divide the squeezed light beams into time bins of time period T, where $1/T$ is sufficiently narrower than the bandwidths of the identical OPOs. Wave-packets of light in each of the time bins represent mutually independent (orthogonal) squeezed states. Second, a series of EPR states separated by time interval T are deterministically created by combining the two squeezed light beams on the first balanced beam-splitter (Step ii). The quantum correlations that manifest from the beam-splitter interaction are represented by links between the nodes (coloured spheres). The nodes here represent the orthogonal wave-packets. Third, the bottom-rail node of the EPR state is delayed for the duration T after passing through a fiber delay line (Step iii). After the delay the top-rail node of each EPR state is synchronised in time with the bottom-rail node of the previous EPR state. By combining the staggered EPR states on the second balanced beam-splitter, each EPR state interacts with the previous and successive EPR states (Step iv). This leads to all of the wave-packets in each of the two rails being connected to neighbouring wave-packets by entanglement links, thereby producing the XEPR state.

The original proposal[25] for using the XEPR state as a resource state for MBQC is inefficient in its use of available squeezing resources. In Fig. 2, we introduce a new, efficient method based on sequential QT. QT in a strict sense is an identity operation on the input quantum state, but it can be generalized to unitary operations by appropriately changing the measurement bases, leading to MBQC. Each QT requires an EPR state and involves two single-mode measurements

4

followed by subsequent phase-space displacement operations that depend on the measurement outcomes. The two circuits of Figure 2a and Figure 2b perform identical operations, due to the parallelism between reversible operations. The resource state in Figure 2b is precisely the XEPR state.

Ideal quadrature-entangled states are simultaneous eigenstates of particular linear combinations of the quadrature operators, called nullifiers[27,28]. For example an ideal EPR state $|\text{EPR}\rangle$, which is the ideal state approximated by the Gaussian state at step ii in Fig. 1a, is specified by the following nullifier relations:

$$\left(\hat{x}^A - \hat{x}^B\right)|\text{EPR}\rangle = 0,$$
$$\left(\hat{p}^A + \hat{p}^B\right)|\text{EPR}\rangle = 0. \tag{1}$$

Here, superscripts A and B denote two wave-packets. In our setup, they refer to the top rail and bottom-rail wave-packets, respectively. $\hat{x}^Q$ and $\hat{p}^Q$ are the quadrature operators of a wave-packet Q, which do not commute for the same wave-packet: $\left[\hat{x}^Q, \hat{p}^R\right] = i\delta_{Q,R}/2$, where $\delta_{Q,R}$ is the Kronecker delta, and $\hbar$ is normalised to $1/2$. While $\hat{x}$ and $\hat{p}$ of a single wave-packet cannot be determined simultaneously due to the Heisenberg uncertainty principle, equation (1) shows that the correlations between the two wave-packets are perfectly determined. More precisely, the quadrature amplitudes $\hat{x}$ of the two wave-packets are perfectly correlated ($x^A = x^B$), and the amplitudes $\hat{p}$ are perfectly anticorrelated ($p^A = -p^B$).

In its ideal form, the XEPR state $|\text{XEPR}\rangle$ generated in our experiment (Fig. 1b) is specified by

$$\left(\hat{x}_k^A + \hat{x}_k^B + \hat{x}_{k+1}^A - \hat{x}_{k+1}^B\right)|\text{XEPR}\rangle = 0,$$
$$\left(\hat{p}_k^A + \hat{p}_k^B - \hat{p}_{k+1}^A + \hat{p}_{k+1}^B\right)|\text{XEPR}\rangle = 0. \tag{2}$$

Here, A and B denote the two independent beams (top and bottom rail, respectively), while $k = 1, 2, \ldots$ represents the temporal index. We consider the XEPR state to be a natural extension of

EPR states because the nullifiers are composed of either $\hat{x}$ or $\hat{p}$ quadratures, but not both. We see that the addition of two quadratures $\hat{x}_k^A + \hat{x}_k^B$ (respectively, $\hat{p}_k^A + \hat{p}_k^B$) at any given time index k have negative (positive) correlations with the difference of the two quadratures $\hat{x}_{k+1}^A - \hat{x}_{k+1}^B$ (respectively, $\hat{p}_{k+1}^A - \hat{p}_{k+1}^B$) at the subsequent time index $k + 1$. The XEPR state is entirely equivalent to a CV cluster state under an appropriate redefinition of quadrature operators ($\hat{x} \to \hat{p}$, $\hat{p} \to -\hat{x}$) for every other temporal mode[28]. Such a redefinition is completely passive and does not change the resource requirements for MBQC using this state, but we choose to call it an XEPR state rather than a CV cluster state because our verification procedure takes advantage on the fact that the ideal nullifiers only involves $\hat{x}$s and $\hat{p}$s.

In reality, the generated XEPR states — and therefore the nullifiers — have excess noise due to the unphysical nature of infinite squeezing. Despite this, the full inseparability of the state can be shown when the resource squeezing level is high enough. The sufficient conditions for fully inseparable entanglement[29] are given by the variances as

$$\left\langle \left(\hat{x}_k^A + \hat{x}_k^B + \hat{x}_{k+1}^A - \hat{x}_{k+1}^B \right)^2 \right\rangle < \frac{1}{2}$$
$$\text{and} \quad \left\langle \left(\hat{p}_k^A + \hat{p}_k^B - \hat{p}_{k+1}^A + \hat{p}_{k+1}^B \right)^2 \right\rangle < \frac{1}{2} \tag{3}$$

for all k, where a bracket $\hat{O}$ ($\langle \hat{O} \rangle$) denotes the expectation value of an operator $\hat{O}$.

The experimental quadrature amplitudes $\hat{x}_k^A$, $\hat{p}_k^A$, $\hat{x}_k^B$ and $\hat{p}_k^B$ of the first 50 wave-packets are plotted in Fig. 3(a–d). We see they are randomly distributed around zero. Linear combinations of the quadrature amplitudes at neighbouring times exhibit quantum correlations as in equation (2) and are shown in Fig. 3(e,f). The amplitudes almost perfectly overlap, showing strong anti-correlations and correlations in both quadrature combinations.

In order to quantify the quantum correlations, we repeat the single-shot generation of the entire XEPR state more than $3,000$ times, allowing us to measure the variances at each temporal position. We then evaluate the multi-partite inseparability criteria given in equation (3). The

6

measurement results are shown in Fig. 4. The variances for the XEPR states are shown by traces (i). The bound of inseparability given in equation (3) corresponds to -3.0 dB, shown by the dashed lines (iii). We see that the experimental XEPR state is clearly below the bound of inseparability in the entangled region for more than $5,000$ temporal positions. Given the dual-rail structure of the XEPR state, the two beams A and B each contain the same number of wave-packets, so that $5,000$ temporal positions corresponds to $10,000$ wave-packets. Vacuum-state inputs are used as references, and traces around 0 dB (ii) show the variances of the nullifiers for the vacuum states.

The mean variances of the first $1,000$ points in the $\hat{x}$ and $\hat{p}$ quadratures are -4.9 ± 0.2 dB and -5.2 ± 0.2 dB, respectively. Note that absolutely no corrections for any losses are performed.

The variances of the XEPR state steadily increase (and therefore the entanglement degrades) with time for technical reasons related to our control scheme. During the data acquisition process we switch off all active feedback control of the optical setup. This is in order to avoid any unwanted noise arising from the feedback that will degrade our measurements. The increase in variance is therefore explained by the relative phase drifts of the entangled state caused by disturbances from the environment.

In summary, we have experimentally demonstrated the generation of ultra-large-scale entangled states in a deterministic fashion. More than $10,000$ wave-packets of light are shown to be fully inseparable in a CV cluster-state configuration. Fault-tolerant quantum computation will additionally require efficient encoding and error correction[27]. Compared to the largest entangled states previously engineered, the number of entangled modes here is larger by three orders of magnitude. Due to their sheer size, regular structure, and deterministic method of creation, we fully expect that these ultra-large-scale states will enable other QIP applications in addition to MBQC.

Methods

The squeezing levels of our OPOs were -6 dB with a bandwidth of 34 MHz. The optical fiber length was 30 m, corresponding to the time duration of the wave-packets $T = 157.5$ ns. Homodyne detection is employed to measure the quadrature amplitudes of each wave-packet. The signals of the homodyne detectors are integrated with the non-overlapping temporally-localised mode functions of the wave-packets.

References

1. Nielsen, M. A. & Chuang, I. L. *Quantum Computation and Quantum Information* (Cambridge Univ. Press, 2000).

2. Raussendorf, R. & Briegel, H. J. A one-way quantum computer. *Phys. Rev. Lett.* **86,** 5188–5191 (2001).

3. Briegel, H. J. & Raussendorf, R. Persistent Entanglement in Arrays of Interacting Particles. *Phys. Rev. Lett.* **86**, 910–913 (2001).

4. Yao, X.-C. *et al.* Observation of eight-photon entanglement. *Nature Photon.* **6,** 225–228 (2012).

5. Su, X. *et al.* Experimental preparation of eight-partite cluster state for photonic qumodes. *Opt. Lett.* **37,** 5178-5180 (2012).

6. Monz, T. *et al.* 14-Qubit Entanglement: Creation and Coherence. *Phys. Rev. Lett.* **106,** 130506 (2011).

7. Zhang, J. & Braunstein, S. L. Continuous-variable Gaussian analog of cluster states. *Phys. Rev. A* **73,** 032318 (2006).

8. Menicucci, N. C. *et al.* Universal Quantum Computation with Continuous-Variable Cluster States. *Phys. Rev. Lett.* **97,** 110501 (2006).

9. Einstein, A., Podolsky, B. & Rosen, N. Can Quantum-Mechanical Description of Physical Reality Be Considered Complete? *Phys. Rev.* **47,** 777–780 (1935).

10. Bell, J. S. On the Einstein-Podolsky-Rosen paradox. *Physics* **1**, 195–200 (1964).

11. Furusawa, A. & van Loock, P. *Quantum Teleportation and Entanglement* (Wiley-VCH, 2011).

12. Bennett, C. H. *et al.* Teleporting an Unknown Quantum State via Dual Classical and Einstein-Podolsky-Rosen Channels. *Phys. Rev. Lett.* **70,** 1895–1899 (1993).

13. Furusawa, A. *et al.* Unconditional quantum teleportation. *Science* **282,** 706–709 (1998).

14. Lee, N. *et al.* Teleportation of Nonclassical Wave Packets of Light. *Science* **332,** 330–333 (2011).

15. Walther, P. *et al.* Experimental one-way quantum computing. *Nature* **434,** 169–176 (2005).

16. Tokunaga, Y. *et al.* Generation of High-Fidelity Four-Photon Cluster State and Quantum-Domain Demonstration of One-Way Quantum Computing. *Phys. Rev. Lett.* **100,** 210501 (2008).

17. Ukai, R. *et al.* Demonstration of Unconditional One-Way Quantum Computations for Continuous Variables. *Phys. Rev. Lett.* **106,** 240504 (2011).

18. Ukai, R., Yokoyama, S., Yoshikawa, J., van Loock, P., Furusawa, A. Demonstration of a Controlled-Phase Gate for Continuous-Variable One-Way Quantum Computation. *Phys. Rev. Lett.* **107,** 250501 (2011).

19. Yukawa, M., Ukai, R., van Loock, P. & Furusawa, A. Experimental generation of four-mode continuous-variable cluster states. *Phys. Rev. A* **78,** 012301 (2008).

20. van Loock, P., Weedbrook, C. & Gu, M. Building Gaussian cluster states by linear optics. *Phys. Rev. A* **76,** 032321 (2007).

21. Armstrong, S. *et al.* Programmable multimode quantum networks. *Nat. Commun.* **3,** 1026 (2012).

22. Pysher, M., Miwa, Y., Shahrokhshahi, R., Bloomer, R. & Pfister, O. Parallel Generation of Quadripartite Cluster Entanglement in the Optical Frequency Comb. *Phys. Rev. Lett.* **107,** 030505 (2011).

23. Roslund, J., de Araújo, R. M., Jiang, S., Fabre, C. & Treps, N. Wavelength-multiplexed quantum networks with ultrafast frequency combs. *Nat. Photon.* **8,** 109 (2014).

24. Menicucci, N. C. Flammia, S. T. & Pfister, O. One-Way Quantum Computing in the Optical Frequency Comb. *Phys. Rev. Lett.* **101,** 130501 (2008).

25. Menicucci, N. C. Temporal-mode continuous-variable cluster states using linear optics. *Phys. Rev. A* **83,** 062314 (2011).

26. Usmani, I., Afzelius, M., de Riedmatten, H. & Gisin, N. Mapping multiple photonic qubits into and out of one solid-state atomic ensemble. *Nat. Commun.* **1,** 12 (2010).

27. Gu, M., Weedbrook, C., Menicucci, N. C. Ralph, T. C. & van Loock, P. "Quantum Computing with Continuous-Variable Clusters," *Phys. Rev. A* **79,** 062318 (2009).

28. Menicucci, N. C. Flammia, S. T. & van Loock, P. Graphical calculus for Gaussian pure states. *Phys. Rev. A* **83,** 042335 (2011).

29. van Loock, P. & Furusawa, A. Detecting genuine multipartite continuous-variable entanglement. *Phys. Rev. A* **67,** 052315 (2003).

Author contributions

S.Y., R.U. and S.A. planned and designed the experiment under the supervision of J.Y., H.Y. and A.F., based on the proposal by N.C.M. S.Y. designed the experimental setup. C.S, T.K. and S.Y. constructed the optical setup, and S.S. built the fiber alignment system. R.U., S.A., N.C.M. and J.Y. formulated the theory. R.U. designed and constructed the data acquisition system. S.A. designed and constructed the digital control system. R.U., S.A., T.K. and S.Y. conducted the data analysis. H.Y. assisted in noise analysis. S.Y. and S.A. wrote the manuscript with assistance from the team.
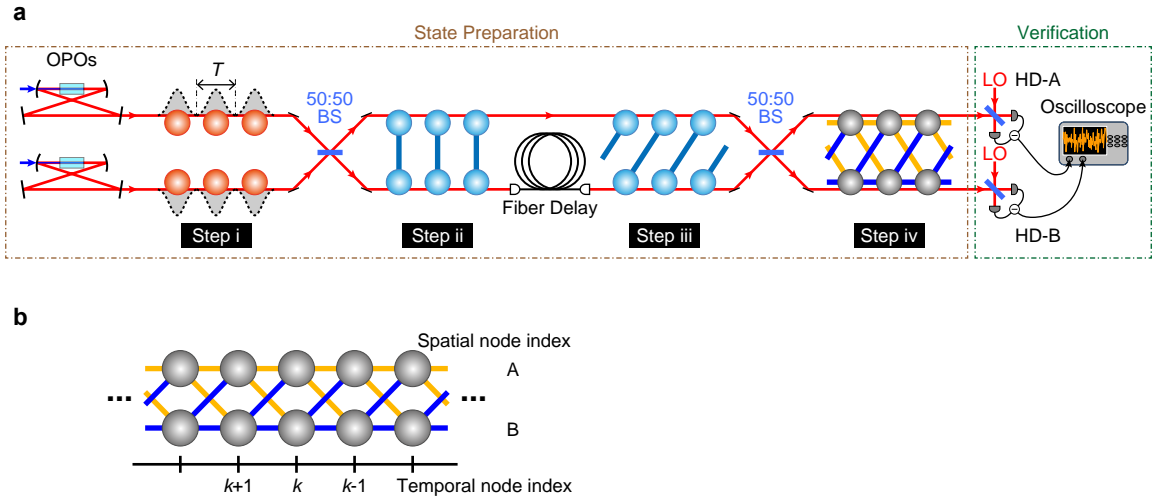
Additional information

Supplementary information is available in the online version of the paper. Preprints and permissions information is available online at www.nature.com/reprints. Correspondence and requests

for materials should be addressed to A.F.

Competing financial interests

The authors declare no competing financial interests.

Figure 1 | **Schematic of the experimental setup and ultra-large-scale XEPR state.**
a, Generation of ultra-large-scale cluster-state entanglement. Squeezed temporal modes are mixed on a beam-splitter to create EPR states, which are then staggered by a fiber delay line. The staggered EPR-state wave-packets are then mixed to generate a continuous graph structure, where each wave-packet is entangled to neighbouring wave-packets. Nodes (coloured spheres) and links between them represent optical wave-packets and entanglement, respectively. Independent quantum states exist in each temporally localised wave-packet with time duration T. OPO, optical parametric oscillator; 50:50 BS, balanced beam-splitter; HD, homodyne detector; LO, local oscillator. **b**, The extended EPR state, equivalent to a CV cluster state up to local phase shifts (redefinition of quadrature operators). See supplementary section 'S2' for full details and graph representation.

13
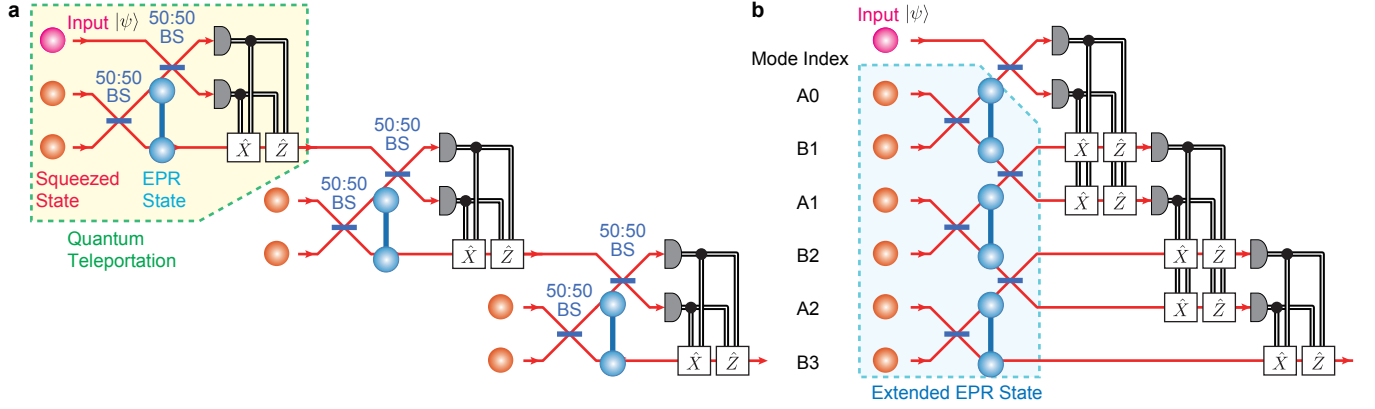
Figure 2 | XEPR states for sequential quantum teleportation.
a, Circuit of standard sequential quantum teleportation. **b**, Circuit of sequential quantum teleportation through the XEPR state. 50:50 BS, balanced beam-splitter; $|\psi\rangle$, arbitrary and unknown quantum state as the input of quantum teleporter; $\hat{X}$ or $\hat{Z}$, phase-space displacement operation based on measurement outcomes.
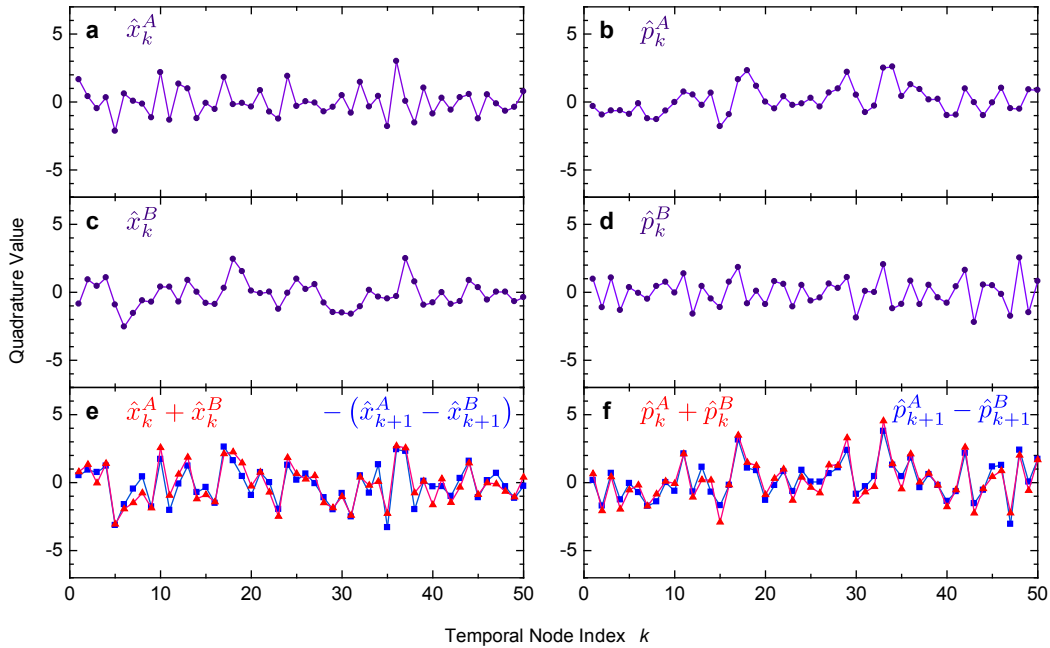
Figure 3 | Measured quantum correlations of the first 50 wave-packets.
a–d, Measured quadrature amplitudes of $\hat{x}_k^A$, $\hat{p}_k^A$, $\hat{x}_k^B$ and $\hat{p}_k^B$ of temporally localised wave-packets at temporal node positions k. They are randomly distributed around zero. **e,f**, Additions and time-shifted subtractions of certain quadratures show quantum correlations displayed by the near perfect overlaps.

14

a $\left\langle(\hat{x}_k^A + \hat{x}_k^B + \hat{x}_{k+1}^A - \hat{x}_{k+1}^B)^2\right\rangle$

b $\left\langle(\hat{p}_k^A + \hat{p}_k^B - \hat{p}_{k+1}^A + \hat{p}_{k+1}^B)^2\right\rangle$
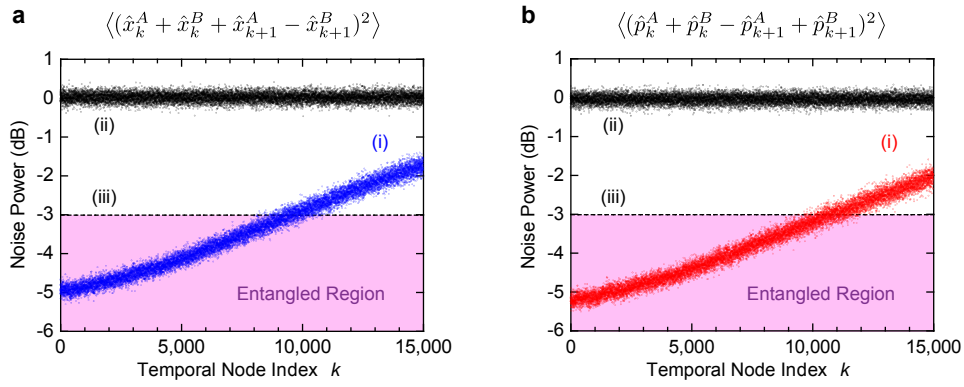
Figure 4 | **Quantum correlations of the XEPR state for the first** $30,000$ **wave-packets.** **a,b**, (i) Measured nullifier variances for the first $15,000$ temporal mode positions ($30,000$ wave-packets in both rails) are shown for the $\hat{x}$ quadrature in blue (**a**) and for the $\hat{p}$ quadrature in red (**b**), as in equation (3). (ii) measured variances for vacuum inputs, used as a reference for noise power. (iii) -3.0 dB lines indicate the bounds of inseparability; data points below this line demonstrate entanglement.

15

Supplementary Information for Ultra-Large-Scale Continuous-Variable Cluster States Multiplexed in the Time Domain

S1   Experimental Setup

Figure S5 shows the schematic of the experimental setup. In this setup, we employ a continuous-wave (CW) Ti:Sapphire laser (SolsTiS-SRX, M Squared Lasers) operating at 860 nm as the primary optical source. The pump laser is a laser-diode-pumped and frequency-doubled Nd:YVO$_4$ laser (Verdi V-10, Coherent). 10 W of the pump beam from the Nd:YVO$_4$ results in 1.9 W output power of the Ti:Sapphire laser.

The 860 nm fundamental beam passes through the optical isolator (ISO; FI850-5SV, Linos) and the electro-optic phase modulator (EOM; PM25, Linos). The phase modulation by the EOM adds 16.5 MHz sideband components which are utilised for locking all the optical cavities via the Pound-Drever-Hall locking technique.

Almost half of the fundamental beam is sent to a second harmonic generator (SHG) and
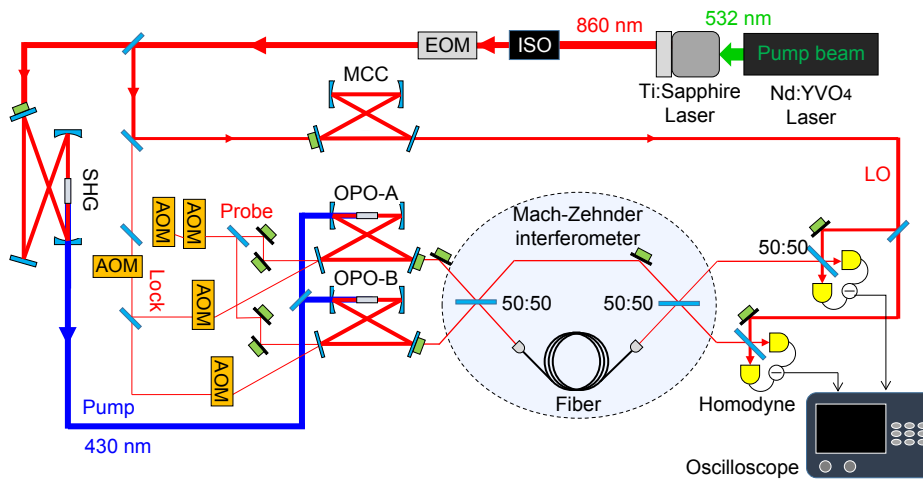
Fig. S5. Experimental setup.

converted to approximately 500 mW of a 430 nm beam. The SHG is a bow-tie cavity consisting of two spherical mirrors (radius of curvature 50 mm), two flat mirrors, and contains a 10 mm $\times$ 3 mm $\times$ 3 mm $KNbO_3$ crystal. Its round trip length is 500 mm, and the input coupler transmissivity is 10%. The rest of the fundamental beam is further split and distributed for controlling the sub-threshold optical parametric oscillators (OPOs), the interferometers, the homodyne detectors, and so on.

The second harmonic from the SHG is injected into the OPOs as their pump beam (100 mW for each OPO) to generate the squeezed vacuum beams, which are the quantum resources for this experiment. The OPO is a bow-tie cavity consisting of two spherical mirrors (radius of curvature 38 mm), two flat mirrors and a 10 mm $\times$ 1 mm $\times$ 1 mm periodically poled $KTiOPO_4$ (PPKTP) crystal. Its round trip length is 230 mm, the half width at half maximum is 17 MHz, the output coupler transmissivities are 14.9% (OPO-A) and 15.4% (OPO-B), and intra cavity losses are 0.41% (OPO-A) and 0.30% (OPO-B). The OPO is locked via the Pound-Drever-Hall locking method by introducing a locking beam which is appropriately frequency-shifted and counter-propagating in the cavity so as to avoid interference with the squeezed vacuum beam.

The squeezed vacuum states are combined by a Mach-Zehnder interferometer (MZI) with asymmetric arm lengths. After the first balanced beam-splitter, they are converted into two-mode EPR states. The EPR states become staggered due to the asymmetric arm lengths. The staggered EPR states are then combined in sequence at the second balanced beam-splitter, forming the extended EPR state.

For the optical delay line to asymmetrise the MZI, we employ an optical fiber. To minimize the insertion loss of the delay line, we employ fiber patchcodes with special anti-reflection (AR) coatings at 860 nm on both ends (PMJ-3A3A-850-5/125-1-2-1-AR2, OZ Optics). We fabricated arbitrary lengths of fiber cables by splicing the patchcodes and bare fibers (SM85-PS-U40A, Fujikura). The lenses for focusing and collimating the beam are single aspheric

lenses with AR coatings (C240TME-B, Thorlabs). Furthermore, in the aim of improving the spatial mode matching between the TEM_{00} in free-space and LP_{01} in PM fibers, we developed a special fiber alignment device (FA1000S, FMD Corporation). As a result, we obtained 92% in the throughput of the entire fiber delay line, which was kept as high as 89% during 6 hours. Since small temperature changes around the fiber cause drastic changes of the optical pass length resulting in the instability of phase locking, the fiber is placed inside a box consisting of heat insulating material and vibration-proofing materials.

The Extended EPR states are measured by homodyne detectors. The two homodyne measurements are performed with balanced beam-splitters and continuous-wave local oscillator (LO) beams. To optimise the spatial mode-matching, the LO beams are first filtered by a separate cavity which is a bow-tie cavity consisting of two spherical mirrors (radius of curvature 38 mm) and two flat mirrors. Its round trip is 230 mm length, finesse is 25, the half width at half maximum is 27 MHz, and the input and output coupler transmissivities are both 5%. Visibilities are above 98% for every pair of signal beams through free space including the LO beams. The average visibility through the fiber is 95%. The propagation efficiencies from the OPOs to the homodyne detectors are 85–96%. The quantum efficiencies of photodiodes (special order, Hamamatsu Photonics) used in homodyne detectors are about 99%, while the bandwidth of the detectors are above 20 MHz. The LO power is set to 10 mW for every homodyne measurement.

The signals from the homodyne detectors in the time-domain are stored by an oscilloscope (DPO 7054, Tektronix). The sampling rate of the oscilloscope is set to 200 MHz in order to sample enough data points in each wave packet. Each frame of 2.5 ms contains $500,000$ points, corresponding to about $30,000$ wave-packets. For each quadrature measurement of each wave-packet we measure $3,000$ frames in order to gather enough statistics to calculate variances. The

quadrature amplitudes are elicited from them by using the temporal mode function $f(t)$.

$$\hat{\xi}_k = \int_{-T/2}^{T/2} \hat{\xi}(t - kT)f(t)\mathrm{d}t, \tag{S4}$$

where $\hat{\xi}_k$ ($\hat{\xi} = \hat{x}, \hat{p}$) are discretized quadratures, $\hat{\xi}(t)$ ($\hat{\xi} = \hat{x}, \hat{p}$) are continuous quadratures from the homodyne detectors, and $f(t)$ is a Gaussian filter $f(t) \propto \mathrm{e}^{-(\Gamma t)^2}$ which is normalised as $\int_{-T/2}^{T/2} |f(t)|^2 \, \mathrm{d}t = 1$. While the bandwidth Γ can be chosen arbitrarily, the interval of the wave-packet T depends on the fiber length. The parameters used here are $T = 157.5$ ns and $\Gamma = 2\pi \times 2.5$ MHz ($1/\Gamma \sim 64$ ns).

It is necessary to lock the relative phases of beams at every point where the beams interfere. For this purpose, we utilise bright laser beams of about 10 μW, which are directed by homodyne detectors. However, their laser noise interferes with our measurement results. To avoid this problem, we switch between data acquisition and feedback control periodically at a switching frequency of 25 Hz. Furthermore, to realise strong and reliable phase locking, we implement a custom-made digital feedback control system via field programmable gate arrays (NI PXI-7853R, National Instruments) in PXI chassis (NI PXI-1033, National Instruments).

S1.1 Animation

An animation can be found at (http://www.alice.t.u-tokyo.ac.jp/Graph-animation.avi) that shows temporal modes propagating through the experimental setup. Figure S6 is provided as a legend for the animation.

S2 Theory

S2.1 Derivation of Extended EPR States

An equivalent linear optics network to our experimental setup is represented in Fig. S7. In this section we derive the expressions of the extended EPR state by following this circuit with both

19
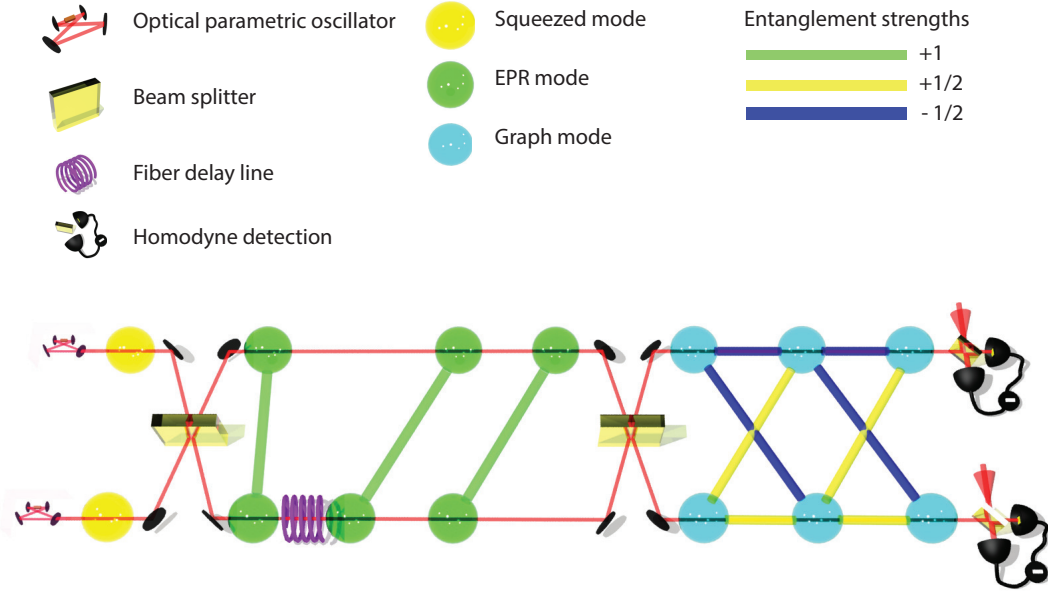
**Fig. S6.** Legend for animation of experimental setup.

Schrödinger and Heisenberg evolutions. In the Schrödinger picture, we assume the ideal case where the resource squeezing levels are infinite. On the other hand we can calculate experimentally realistic expressions in the Heisenberg picture.

S2.1.1 Schrödinger Picture in the Ideal Case

Here we utilise infinite squeezing for simplicity. As per the following calculations with Schrödinger evolution, the output state is a simultaneous eigenstate of nullifiers. First, there are position and momentum eigenstates with zero eigenvalue in each temporal location k. Each row in Fig. S7 shows the spatial mode index which the temporal-mode method would correspond to. The ket vector $|\mathrm{i}\rangle$ in step (i) is represented as

$$|\mathrm{i}\rangle = \prod_k |x=0\rangle_k^A |p=0\rangle_k^B \propto \prod_k \int |x=0\rangle_k^A |x=a_k\rangle_k^B \, \mathrm{d}a_k. \qquad (S5)$$

Note that we omit the interval of an integral in this text when the integral interval is from $-\infty$ to ∞. Second, x and p eigenstates in each temporal location are combined by the first beam-

20
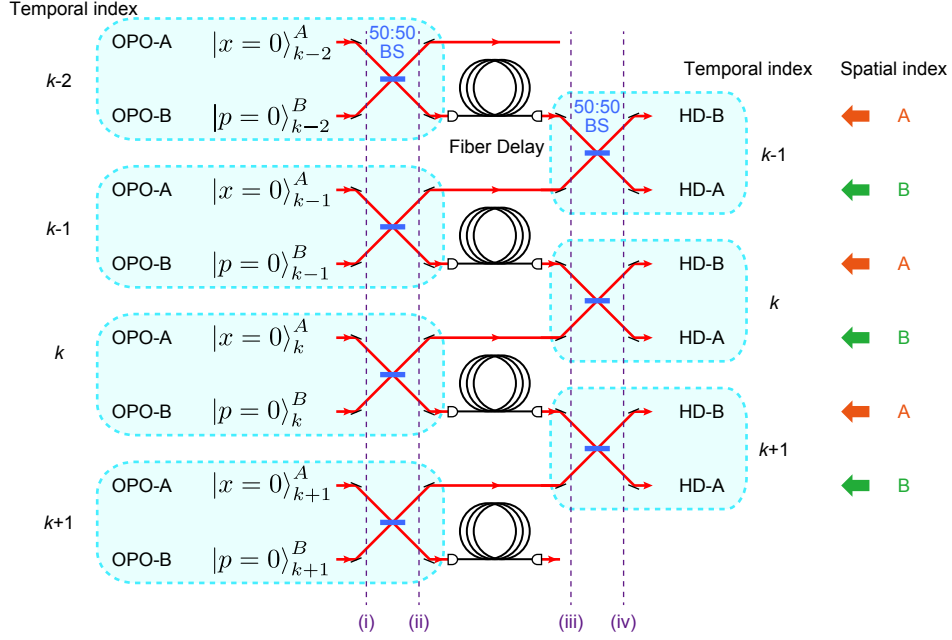
Fig. S7. The equivalent quantum circuit to the temporal-mode method setup.

splitters. Here, the beam-splitter operator $\hat{B}_{i,j}$ for mode i and j is defined as $\hat{B}_{i,j}|x = a\rangle_i|x = b\rangle_j = |x = (a+b)/\sqrt{2}\rangle_i|x = (-a+b)/\sqrt{2}\rangle_j$. Therefore $|\text{ii}\rangle$ becomes

$$|\text{ii}\rangle = \prod_k \hat{B}_{Ak,Bk}|\text{i}\rangle \propto \prod_k \int \left|x = \tfrac{a_k}{\sqrt{2}}\right\rangle_k^A \left|x = \tfrac{a_k}{\sqrt{2}}\right\rangle_k^B \mathrm{d}a_k. \tag{S6}$$

Then an optical delay is implemented to spatial mode B. It is equivalent to a delay in the temporal mode index: $k \to k+1$,

$$|\text{iii}\rangle \propto \prod_k \int \left|x = \tfrac{a_k}{\sqrt{2}}\right\rangle_k^A \left|x = \tfrac{a_k}{\sqrt{2}}\right\rangle_{k+1}^B \mathrm{d}a_k = \int \prod_k \left|x = \tfrac{a_k}{\sqrt{2}}\right\rangle_k^A \left|x = \tfrac{a_{k-1}}{\sqrt{2}}\right\rangle_k^B \mathrm{d}a_k. \tag{S7}$$

Finally, the beams are combined on the second beam-splitters, giving

$$|\text{iv}\rangle = \prod_k \hat{B}_{Bk,Ak}|\text{iii}\rangle \propto \int \prod_k \left|x = \tfrac{1}{2}(a_k - a_{k-1})\right\rangle_k^A \left|x = \tfrac{1}{2}(a_k + a_{k-1})\right\rangle_k^B \mathrm{d}a_k. \tag{S8}$$

In the same manner the expressions in the p basis can also be calculated as

$$|\text{iv}\rangle \propto \int \prod_k \left|p = \tfrac{1}{2}(b_k + b_{k-1})\right\rangle_k^A \left|p = \tfrac{1}{2}(b_k - b_{k-1})\right\rangle_k^B \mathrm{d}b_k. \tag{S9}$$

21

Since the output extended EPR state $|\text{XEPR}\rangle$ is equal to $|\text{iv}\rangle$, the nullifiers obviously become zero as

$$\left(\hat{x}_k^A + \hat{x}_k^B + \hat{x}_{k+1}^A - \hat{x}_{k+1}^B\right)|\text{XEPR}\rangle = 0, \tag{S10}$$

$$\left(\hat{p}_k^A + \hat{p}_k^B - \hat{p}_{k+1}^A + \hat{p}_{k+1}^B\right)|\text{XEPR}\rangle = 0. \tag{S11}$$

S2.1.2 Heisenberg Evolution with Finite Squeezing

In the Heisenberg evolution, the variances of nullifiers in the case of finite resource squeezing levels can be calculated. The complex amplitudes $\hat{a}_k^{A(\text{i})}$ and $\hat{a}_k^{B(\text{i})}$ of the initial state in step (i) are represented as

$$\text{(i)} \qquad \hat{a}_k^{A(\text{i})} = \text{e}^{-r_A}\hat{x}_k^{A(0)} + i\,\text{e}^{r_A}\hat{p}_k^{A(0)}, \qquad \hat{a}_k^{B(\text{i})} = \text{e}^{r_B}\hat{x}_k^{B(0)} + i\,\text{e}^{-r_B}\hat{p}_k^{B(0)}, \tag{S12}$$

where $\text{e}^{-r_A}\hat{x}_k^{A(0)}$ and $\text{e}^{-r_B}\hat{p}_k^{B(0)}$ are the squeezed quadratures of the k-th squeezed state in the spatial location A and B, respectively. So we have

$$\left\langle\hat{x}_k^{A(0)}\right\rangle = \left\langle\hat{p}_k^{A(0)}\right\rangle = \left\langle\hat{x}_k^{B(0)}\right\rangle = \left\langle\hat{p}_k^{B(0)}\right\rangle = 0, \tag{S13}$$

$$\left\langle\left(\hat{x}_k^{A(0)}\right)^2\right\rangle = \left\langle\left(\hat{p}_k^{A(0)}\right)^2\right\rangle = \left\langle\left(\hat{x}_k^{B(0)}\right)^2\right\rangle = \left\langle\left(\hat{p}_k^{B(0)}\right)^2\right\rangle = \frac{1}{4}. \tag{S14}$$

After combining the terms through the action of a beam-splitter they become

$$\text{(ii)} \qquad \begin{pmatrix}\hat{a}_k^{A(\text{ii})}\\[2pt]\hat{a}_k^{B(\text{ii})}\end{pmatrix} = \hat{B}_{Ak,Bk}^{\dagger}\begin{pmatrix}\hat{a}_k^{A(\text{i})}\\[2pt]\hat{a}_k^{B(\text{i})}\end{pmatrix}\hat{B}_{Ak,Bk} = \frac{1}{\sqrt{2}}\begin{pmatrix}1 & 1\\-1 & 1\end{pmatrix}\begin{pmatrix}\hat{a}_k^{A(\text{i})}\\[2pt]\hat{a}_k^{B(\text{i})}\end{pmatrix}. \tag{S15}$$

Subsequently, the of optical delay for mode B is represented as

$$\text{(iii)} \qquad \hat{a}_k^{A(\text{iii})} = \hat{a}_k^{A(\text{ii})}, \qquad \hat{a}_k^{B(\text{iii})} = \hat{a}_{k-1}^{B(\text{ii})}. \tag{S16}$$

Finally, by combining them on the last beam-splitter the final complex amplitudes of the output state are given:

$$\begin{aligned}
\text{(iv)} \qquad \begin{pmatrix}\hat{a}_k^{B(\text{iv})}\\[2pt]\hat{a}_k^{A(\text{iv})}\end{pmatrix} &= \hat{B}_{Bk,Ak}^{\dagger}\begin{pmatrix}\hat{a}_k^{B(\text{iii})}\\[2pt]\hat{a}_k^{A(\text{iii})}\end{pmatrix}\hat{B}_{Bk,Ak} = \frac{1}{\sqrt{2}}\begin{pmatrix}1 & 1\\-1 & 1\end{pmatrix}\begin{pmatrix}\hat{a}_k^{B(\text{iii})}\\[2pt]\hat{a}_k^{A(\text{iii})}\end{pmatrix}\\[6pt]
&= \frac{1}{2}\begin{pmatrix}\hat{a}_k^{A(\text{i})} + \hat{a}_k^{B(\text{i})} - \hat{a}_{k-1}^{A(\text{i})} + \hat{a}_{k-1}^{B(\text{i})}\\[2pt]\hat{a}_k^{A(\text{i})} + \hat{a}_k^{B(\text{i})} + \hat{a}_{k-1}^{A(\text{i})} - \hat{a}_{k-1}^{B(\text{i})}\end{pmatrix},
\end{aligned} \tag{S17}$$

22

Since $\hat{a}_k^A = \hat{a}_k^{A(\text{iv})}$ and $\hat{a}_k^B = \hat{a}_k^{B(\text{iv})}$, the ideal nullifiers of the extended EPR state are expressed as

$$\hat{x}_k^A + \hat{x}_k^B + \hat{x}_{k+1}^A - \hat{x}_{k+1}^B = 2\,\text{e}^{-r_A}\hat{x}_k^{A(0)}, \tag{S18}$$

$$\hat{p}_k^A + \hat{p}_k^B - \hat{p}_{k+1}^A + \hat{p}_{k+1}^B = 2\,\text{e}^{-r_B}\hat{p}_k^{B(0)}. \tag{S19}$$

Therefore, we can calculate the nullifier variances which determine the theoretical value of the inseparable condition as shown in the main text [Eq. (3)],

$$\left\langle \left(\hat{x}_k^A + \hat{x}_k^B + \hat{x}_{k+1}^A - \hat{x}_{k+1}^B\right)^2 \right\rangle = \text{e}^{-2r_A} < \frac{1}{2}, \tag{S20}$$

$$\text{and} \quad \left\langle \left(\hat{p}_k^A + \hat{p}_k^B - \hat{p}_{k+1}^A + \hat{p}_{k+1}^B\right)^2 \right\rangle = \text{e}^{-2r_B} < \frac{1}{2}. \tag{S21}$$

This shows that the sufficient condition for inseparability is satisfied when -3 dB resource squeezing in each OPO is available.

S2.2 Inseparability Criteria for Extended EPR States

Here, we discuss sufficient conditions of entanglement for the extended EPR states, based on the van Loock-Furusawa inseparability criteria[29]. We consider all of the cases where an approximate extended EPR state is separable into two subsystems S_1 and S_2. A necessary condition of separability is obtained as an inequality for each case. If all of the separable cases are denied by not satisfying the inequalities, the state is proved to be in an entangled state with full inseparability.

First, we consider the combinations of four nodes $\{A_k, B_k, A_{k+1}, B_{k+1}\}$ distributed into the two subsystems. When all of the four are not distributed into either subsystem, the possible cases are as below. Here we abbreviate the nullifiers as $\hat{X}_k \equiv \hat{x}_k^A + \hat{x}_k^B + \hat{x}_{k+1}^A - \hat{x}_{k+1}^B$ and $\hat{P}_k \equiv \hat{p}_k^A + \hat{p}_k^B - \hat{p}_{k+1}^A + \hat{p}_{k+1}^B$.

- Case: $\{A_k\} \subset S_1$, $\{B_k, A_{k+1}, B_{k+1}\} \subset S_2$.

The addition of nullifier variances always satisfies the following inequality:

$$\langle \hat{X}_k^2 \rangle + \langle \hat{P}_k^2 \rangle \geq \frac{1}{2} \left(|1| + |1 - 1 - 1| \right) = 1. \tag{S22}$$

- Case: $\{B_k\} \subset S_1$, $\{A_k, B_k, B_{k+1}\} \subset S_2$.

  The addition of nullifier variances always satisfies the following inequality:

$$\langle \hat{X}_k^2 \rangle + \langle \hat{P}_k^2 \rangle \geq \frac{1}{2} \left(|1| + |1 - 1 - 1| \right) = 1. \tag{S23}$$

- Case: $\{A_{k+1}\} \subset S_1$, $\{A_k, B_k, B_{k+1}\} \subset S_2$.

  The addition of nullifier variances always satisfies the following inequality:

$$\langle \hat{X}_k^2 \rangle + \langle \hat{P}_k^2 \rangle \geq \frac{1}{2} \left(|-1| + |1 + 1 - 1| \right) = 1. \tag{S24}$$

- Case: $\{B_{k+1}\} \subset S_1$, $\{A_k, B_k, A_{k+1}\} \subset S_2$.

  The addition of nullifier variances always satisfies the following inequality:

$$\langle \hat{X}_k^2 \rangle + \langle \hat{P}_k^2 \rangle \geq \frac{1}{2} \left(|-1| + |1 + 1 - 1| \right) = 1. \tag{S25}$$

- Case: $\{A_k, B_k\} \subset S_1$, $\{A_{k+1}, B_{k+1}\} \subset S_2$.

  The addition of nullifier variances always satisfies the following inequality:

$$\langle \hat{X}_k^2 \rangle + \langle \hat{P}_k^2 \rangle \geq \frac{1}{2} \left(|1 + 1| + |-1 - 1| \right) = 2. \tag{S26}$$

- Case: $\{A_k, A_{k+1}\} \subset S_1$, $\{B_k, B_{k+1}\} \subset S_2$.

  The addition of nullifier variances always satisfies the following inequality:

$$\langle \hat{X}_k^2 \rangle + \langle \hat{P}_{k+1}^2 \rangle \geq \frac{1}{2} \left(|1| + |-1| \right) = 1. \tag{S27}$$

- Case: $\{A_k, B_{k+1}\} \subset S_1$, $\{B_k, A_{k+1}\} \subset S_2$.

The addition of nullifier variances always satisfies the following inequality:

$$\left\langle \hat{X}_k^2 \right\rangle + \left\langle \hat{P}_{k+1}^2 \right\rangle \geq \frac{1}{2} \left(|-1| + |1| \right) = 1. \tag{S28}$$

Therefore, when the inequalities $\left\langle \hat{X}_k^2 \right\rangle + \left\langle \hat{P}_k^2 \right\rangle < 1$ and $\left\langle \hat{X}_k^2 \right\rangle + \left\langle \hat{P}_{k+1}^2 \right\rangle < 1$ are satisfied, any of the seven inequalities (S22)–(S28) is not satisfied, which means that the four nodes $\{A_k, B_k, A_{k+1}, B_{k+1}\}$ are not separable into two subsystem S_1 and S_2.

Then, we apply the same discussion for all temporal indices k. When the inequalities $\left\langle \hat{X}_k^2 \right\rangle + \left\langle \hat{P}_k^2 \right\rangle < 1$ and $\left\langle \hat{X}_k^2 \right\rangle + \left\langle \hat{P}_{k+1}^2 \right\rangle < 1$ are satisfied for all k, any partitioning of the whole system is denied, which means that all nodes are entangled. We may take a more severe but simpler sufficient condition for entanglement as

$$\left\langle \hat{X}_k^2 \right\rangle < \frac{1}{2} \quad \text{and} \quad \left\langle \hat{P}_k^2 \right\rangle < \frac{1}{2}, \tag{S29}$$

for all k, which is shown in Eq. (3) of the main text.

S2.3   Graph Correspondence

In this section, we discuss the intuitive representation of the extended EPR state in terms of the graphical calculus for Gaussian pure states[28]. Every N-mode zero-mean Gaussian pure state can be uniquely represented by an undirected complex-weighted graph $\mathbf{Z}$, whose imaginary part (i.e., that of the adjacency matrix for the graph) is positive definite. (In what follows, we make no distinction between a graph and its adjacency matrix.) The graph $\mathbf{Z}$ shows up directly in the position-space wavefunction for the corresponding state $|\psi_{\mathbf{Z}}\rangle$ (with $\hbar = \frac{1}{2}$):

$$_x\langle \mathbf{s} | \psi_{\mathbf{Z}} \rangle = \psi_{\mathbf{Z}}(\mathbf{s}) \propto \exp\left[i\mathbf{s}^{\mathrm{T}} \mathbf{Z} \mathbf{s} \right]. \tag{S30}$$

Any Gaussian pure state $|\psi_{\mathbf{Z}}\rangle$ satisfies a set of exact nullifier relations based on its associated complex matrix $\mathbf{Z}$ (ref. 28):

$$(\hat{\mathbf{p}} - \mathbf{Z}\hat{\mathbf{x}})\,|\psi_{\mathbf{Z}}\rangle = \mathbf{0}, \tag{S31}$$

where $\hat{\mathbf{p}}$ and $\hat{\mathbf{x}}$ are column vectors of momentum and position operators, respectively. The special case of the N-mode ground state ($\mathbf{Z}_{\text{ground}} = i\mathbf{I}$) is easy to verify by noting that the vector of nullifiers in that case is just the vector of annihilation operators.

The extended EPR state is exactly the state originally proposed by Menicucci in ref. 25. In that proposal, it was shown that such a state is locally equivalent (up to phase shifts on half the modes) to a CV cluster state, which is a universal resource for measurement-based quantum computing with continuous variables[8,27]. Since measurement-based quantum computation requires the ability to do homodyne detection of any (rotated) quadrature, plus photon counting[27], the phase shifts required to transform the generated state (the extended EPR state) into a CV cluster state do not need to be physically performed on the state after generation. Instead, one can account for them entirely just by updating the measurement-based protocol to be implemented (i.e., redefine quadratures $\hat{x} \to \hat{p}$ and $\hat{p} \to -\hat{x}$ on the appropriate modes)[25]. Because of this equivalence, the original proposal[25] used a simplified graphical calculus that blurred the distinction between the extended EPR state and corresponding CV cluster state since the two were, for quantum computational purposes, effectively the same resource. The distinction between these states turns out to make a huge difference, however, when one tries to experimentally characterize the generated state. In this case, it is much easier to work with the mathematics of the extended EPR state.

For clarity and completeness, here we present the full complex-weighted graph $\mathbf{Z}_E$ (ref. 28) corresponding to the extended EPR state originally proposed in ref. 25 and reported on in this work:
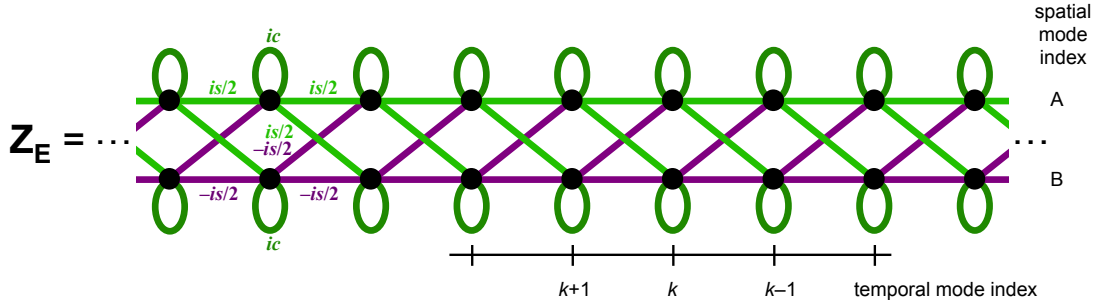
Fig. S8. The full graph[28] for the extended EPR state.

In this graph, $c = \cosh 2r$ and $s = \sinh 2r$, with r being the initial squeezing parameter of the states emitted by the OPO. (See ref. 28 for more details on such graphs.) The green (purple) edges have positive- (negative-)imaginary weight $\pm\frac{i}{2}\sinh 2r$, and the green self-loops have positive-imaginary weight $i\cosh 2r$. This state can be transformed, by $-\frac{\pi}{2}$ phase shifts on both modes of all odd (or all even) time indices, into the following CV cluster state $\mathbf{Z}_C$ (ref. 25):
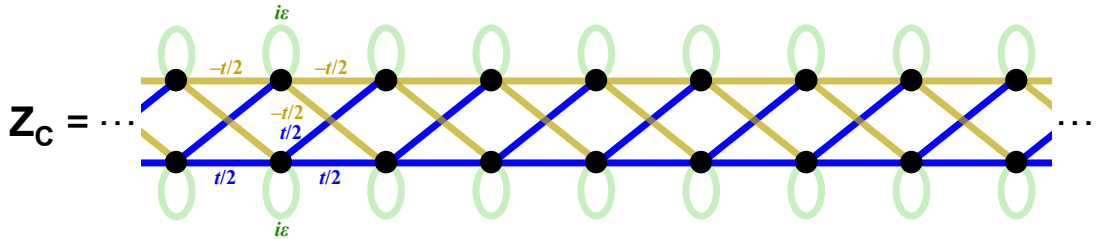
Fig. S9. The full graph[28] for the CV cluster state obtained by phase shifting both spatial modes in every other time index of the extended EPR state.

In this graph, $t = \tanh 2r$ and $\varepsilon = \operatorname{sech} 2r$. The blue (yellow) edges have positive- (negative-)real weight $\pm\frac{1}{2}\tanh 2r$, and the green self-loops have positive-imaginary weight $i\cosh 2r$. Darker colours indicate larger magnitude of the corresponding edge weight. In the large-squeezing limit, $t = \tanh 2r \to 1$, and $\varepsilon = \operatorname{sech} 2r \to 0$, which allows us to define an unphysical, ideal CV cluster-state graph **G** to which $\mathbf{Z}_C$ is a physical approximation:
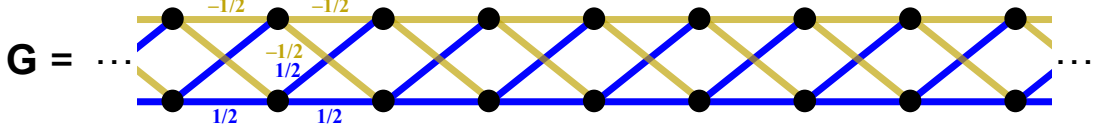
Fig. S10. The ideal CV cluster-state graph in the limit $r \to \infty$.

Notice that

$$\mathbf{Z}_E = i(\cosh 2r)\mathbf{I} - i(\sinh 2r)\mathbf{G}, \tag{S32}$$

$$\mathbf{Z}_C = i(\operatorname{sech} 2r)\mathbf{I} + (\tanh 2r)\mathbf{G}. \tag{S33}$$

The crucial properties of $\mathbf{G}$ that enable such a simple connection between $\mathbf{Z}_E$, $\mathbf{Z}_C$, and $\mathbf{G}$ are (a) that $\mathbf{G}$ is bipartite and (b) that $\mathbf{G}$ is self-inverse (i.e., $\mathbf{G}^2 = \mathbf{I}$ as a matrix). These mathematical properties allow all three of these graphs to be visually similar.

With this simplification in hand, we can derive new nullifier relations for $\mathbf{Z}_E$ in terms of $\mathbf{G}$. We start by observing that premultiplying both sides of Eq. (S31) by $-\mathbf{Z}^{-1}$ gives the additional exact nullifier relation

$$\left(\hat{\mathbf{x}} - \mathbf{Z}^{-1}\hat{\mathbf{p}}\right) |\psi_{\mathbf{Z}}\rangle = \mathbf{0}. \tag{S34}$$

Substituting $\mathbf{Z} \to \mathbf{Z}_E$ [Eq. (S32)] and noting that $\mathbf{Z}_E^{-1} = -i(\cosh 2r)\mathbf{I} - i(\sinh 2r)\mathbf{G}$, we have the two exact nullifier relations

$$[\hat{\mathbf{p}} - (ic\mathbf{I} - is\mathbf{G})\hat{\mathbf{x}}] |\psi_{\mathbf{Z}_E}\rangle = \mathbf{0},$$
$$[\hat{\mathbf{x}} + (ic\mathbf{I} + is\mathbf{G})\hat{\mathbf{p}}] |\psi_{\mathbf{Z}_E}\rangle = \mathbf{0}. \tag{S35}$$

By premultiplying by $\pm i\varepsilon$, respectively, we obtain

$$[i\varepsilon\hat{\mathbf{p}} + (\hat{\mathbf{x}} - t\mathbf{G}\hat{\mathbf{x}})] |\psi_{\mathbf{Z}_E}\rangle = \mathbf{0},$$
$$[-i\varepsilon\hat{\mathbf{x}} + (\hat{\mathbf{p}} + t\mathbf{G}\hat{\mathbf{p}})] |\psi_{\mathbf{Z}_E}\rangle = \mathbf{0}. \tag{S36}$$

28

In the large-squeezing limit ($r \to \infty$), $\varepsilon \to 0$ and $t \to 1$, and we have the following approximate nullifiers for the extended EPR state:

$$(\hat{\mathbf{x}} - \mathbf{G}\hat{\mathbf{x}}) \left| \psi_{\mathbf{Z}_E} \right\rangle \xrightarrow{r \to \infty} \mathbf{0},$$

$$(\hat{\mathbf{p}} + \mathbf{G}\hat{\mathbf{p}}) \left| \psi_{\mathbf{Z}_E} \right\rangle \xrightarrow{r \to \infty} \mathbf{0}. \tag{S37}$$

This is the state we have created. For completeness, however, we can compare these to the exact and approximate nullifiers for the associated CV cluster state $\left| \psi_{\mathbf{Z}_C} \right\rangle$ obtained by phase shifting particular nodes as described above (either actively or by simply redefining quadratures used for the measurements). Substituting $\mathbf{Z} \to \mathbf{Z}_C$ [Eq. (S33)] and noting that $\mathbf{Z}_C^{-1} = -i(\operatorname{sech} 2r)\mathbf{I} + (\tanh 2r)\mathbf{G}$, the exact nullifiers are

$$(-i\varepsilon\hat{\mathbf{x}} + \hat{\mathbf{p}} - t\mathbf{G}\hat{\mathbf{x}}) \left| \psi_{\mathbf{Z}_C} \right\rangle = \mathbf{0},$$

$$(i\varepsilon\hat{\mathbf{p}} + \hat{\mathbf{x}} - t\mathbf{G}\hat{\mathbf{p}}) \left| \psi_{\mathbf{Z}_C} \right\rangle = \mathbf{0}, \tag{S38}$$

which, in the large-squeezing limit, reduce to the following approximate nullifiers:

$$(\hat{\mathbf{p}} - \mathbf{G}\hat{\mathbf{x}}) \left| \psi_{\mathbf{Z}_C} \right\rangle \xrightarrow{r \to \infty} \mathbf{0},$$

$$(\hat{\mathbf{x}} - \mathbf{G}\hat{\mathbf{p}}) \left| \psi_{\mathbf{Z}_C} \right\rangle \xrightarrow{r \to \infty} \mathbf{0}. \tag{S39}$$

Once again, these simple and symmetric expressions in terms of $\mathbf{G}$ are unusual and only possible because $\mathbf{G}$ is bipartite and self-inverse[28].

S2.4 Equivalence to Sequential Teleportation-based Quantum Computation Circuit

In reference 25, Menicucci proposed that by erasing half of the state (one rail), the cluster states can be used as resources for measurement-based quantum computation (MBQC). However, erasing half of the state is a wasteful process and it is experimentally hard to perform the necessary feedforwards to future and past modes in the time axis. Here, we show that the

29

extended EPR state is a resource for MBQC, and that we can fully utilise every degree of freedom without erasing half of the state. We devise a much more efficient method of using this resource state for quantum computation than the method originally proposed in ref. 25, in terms of its use of the available squeezing resources. Specifically, arbitrary Gaussian operation may be implemented by only 4 measurements, which is more efficient than the 8 measurements necessary with the original method[30]. Furthermore, we show that non-Gaussian operations may be performed on the extended EPR state by introducing non-Gaussian measurements, leading to one-mode universal MBQC.

S2.4.1 Gaussian Operation

First of all, let us consider the quantum teleportation-based circuit shown in Fig. S11. The resource EPR state is generated by combining position and momentum eigenstates via the first beam-splitter. After the input state $|\psi\rangle$ is coupled via a second beam-splitter, two observables $\hat{a}_{in}(\theta_1)$ and $\hat{a}_A(\theta_2)$ $(\hat{a}(\theta) = \hat{x}\cos\theta + \hat{p}\sin\theta)$ are measured, giving the measurement results t_1 and t_2. Then, the corresponding feedforward operations $\hat{X}\big(\sqrt{2}(t_1\sin\theta_2 - t_2\sin\theta_1)/\sin\theta_-\big)$ and $\hat{Z}\big(\sqrt{2}(t_1\cos\theta_2 - t_2\cos\theta_1)/\sin\theta_-\big)$ are performed on the remaining mode, where $\hat{X}(s) = \mathrm{e}^{-2is\hat{p}}$ and $\hat{Z}(s) = \mathrm{e}^{2is\hat{x}}$ are the position and momentum displacement operators, and $\theta_\pm$ is $\theta_\pm = \theta_1 \pm \theta_2$. The resulting ket vector $|out\rangle$ becomes

$$|out\rangle = \hat{R}\left(-\theta_+/2 + \pi/2\right)\hat{S}\left(\log\tan(\theta_-/2)\right)\hat{R}\left(-\theta_+/2\right)|\psi\rangle. \tag{S40}$$
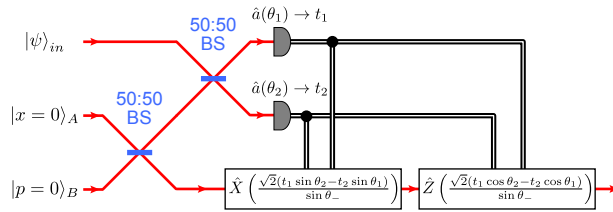
**Fig. S11.** Teleportation-based circuit
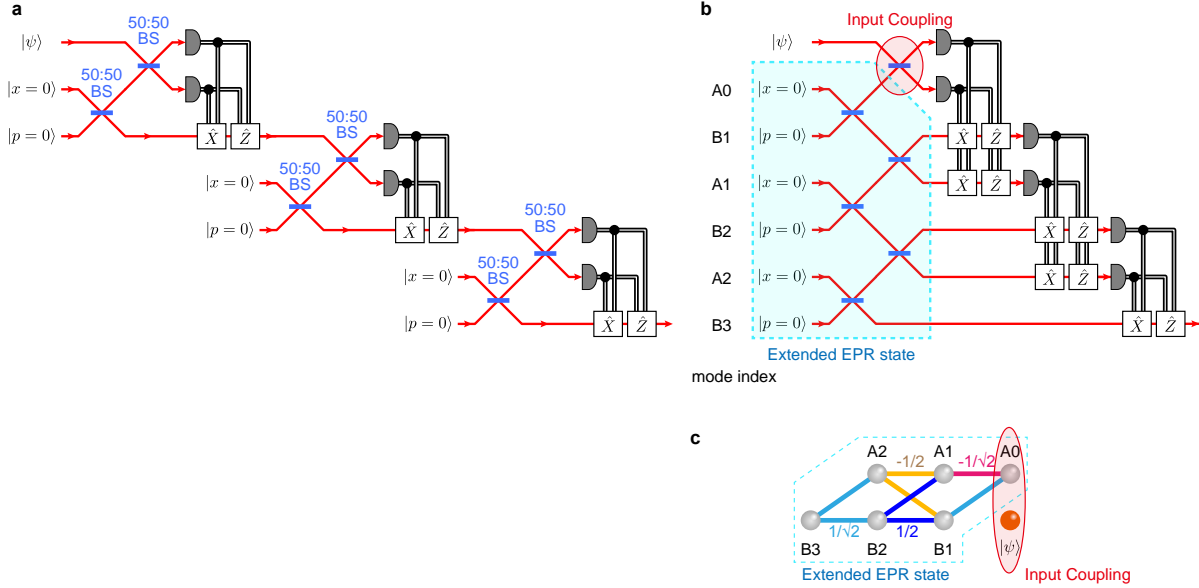
Fig. S12. The resource for MBQC with extended EPR states. **a**, Sequential teleportation circuit. **b**, Equivalent circuit. **c**, Abstract illustration of sequential teleportation with an extended EPR state.

Here, $\hat{R}(\theta) = \mathrm{e}^{i\theta(\hat{x}^2+\hat{p}^2)}$ and $\hat{S}(r) = \mathrm{e}^{ir(\hat{x}\hat{p}+\hat{p}\hat{x})}$ are the θ rotation operator and squeezing operator, respectively, in phase space.

We may combine this teleportation-based circuit sequentially as shown in Fig. S12a. It can be experimentally realised by modifying our experimental setup as shown in Fig. S13, where the input-output coupling port is realised by a switching device to a Mach-Zehnder interferometer containing a configurable phase-shifter. In Fig. S12a, the input-coupling beam-splitters and displacement operators can be exchanged as $\hat{B}_{i,j}\hat{X}_i(t) = \hat{X}_i(t/\sqrt{2})\hat{X}_j(-t/\sqrt{2})\hat{B}_{i,j}$ and $\hat{B}_{i,j}\hat{Z}_i(t) = \hat{Z}_i(t/\sqrt{2})\hat{Z}_j(-t/\sqrt{2})\hat{B}_{i,j}$. As a result, an equivalent circuit is Fig. S12b. Here, in the region enclosed by the dotted line, is the part of the circuit that creates the extended EPR state, which is represented as a graph as shown in Fig. S12c. This shows that the extended EPR state can be used as a resource for MBQC. Therefore, by adding input-coupling, measurement and feedforward optics to our setup, it will become a MBQC circuit.
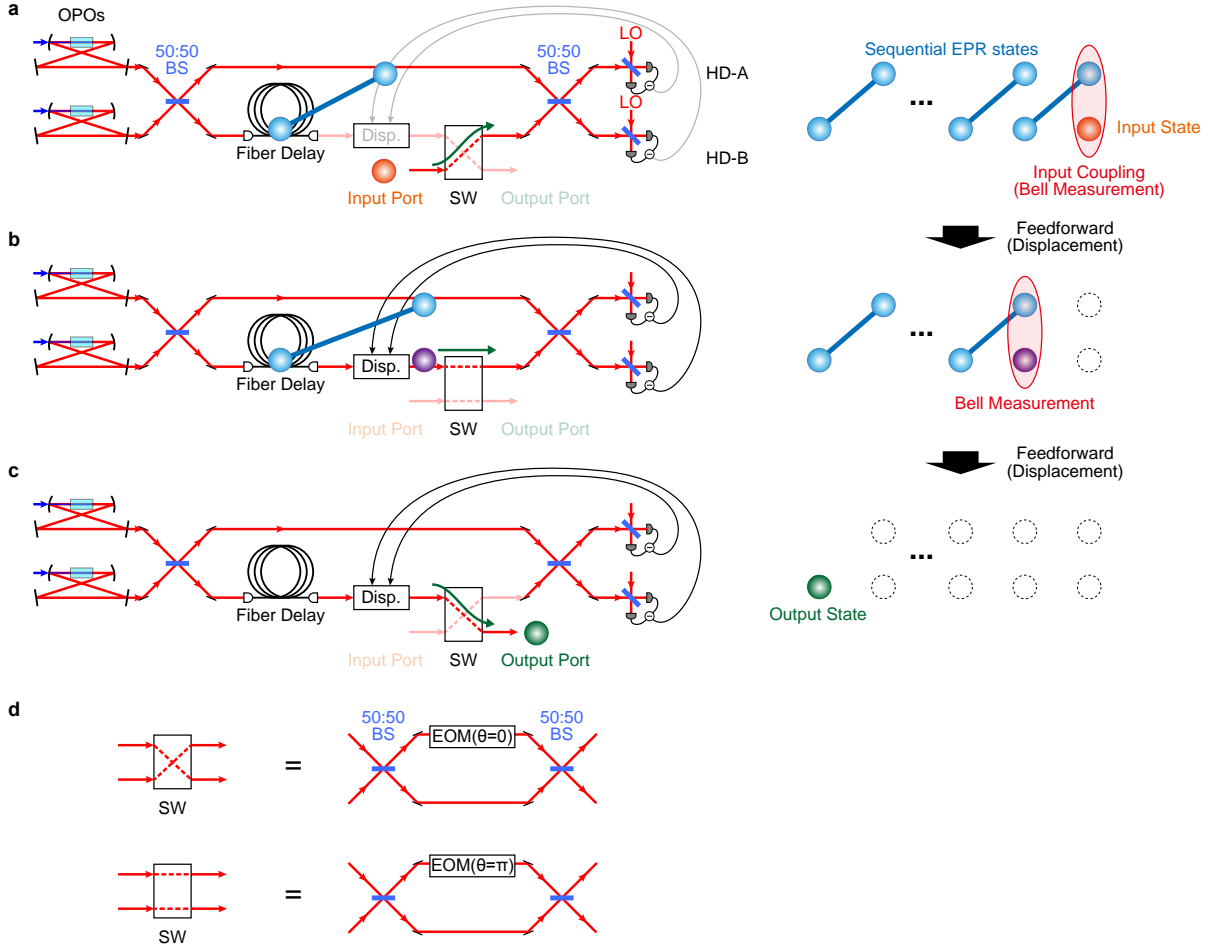
Fig. S13. Experimental setup (left) and abstract illustration (right) for MBQC with extended EPR states. **a**, Input coupling. **b**, Sequential MBQC. **c**, Output. **d**, Switching (SW) device with Mach-Zehnder interferometer including electro optical modulator (EOM).

S2.4.2   Non-Gaussian Operation

Non-Gaussian operations may also be implemented by using the teleportation-based circuit shown in Fig. S14. It is derived in the following way. The ket vector after input coupling is represented as

$$
\hat{B}_{in,A}|\psi\rangle_{in} \otimes \left(\hat{B}_{A,B}|x=0\rangle_A|p=0\rangle_B \right)
$$
$$
\propto \int dt_x|x=t_x\rangle_{in}\hat{X}_A(t_x)\hat{X}_B(\sqrt{2}\,t_x) \otimes \left(\int d\xi\,\psi(\xi)|x=-\sqrt{2}\,\xi\rangle_A|x=-\xi\rangle_B \right). \quad \text{(S41)}
$$

32
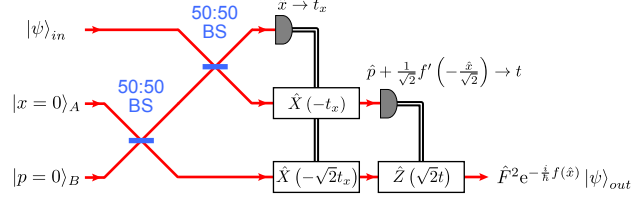
Fig. S14. Teleportation-based non-Gaussian operation circuit

Therefore, by measuring $\hat{x}$ on the input mode giving measurement results t_x, and performing the displacement operation $\hat{X}_A(-t_x)$ and $\hat{X}_B(-\sqrt{2}\,t_x)$, the resulting state becomes $\int \mathrm{d}\xi\,\psi(\xi)\big|x = -\sqrt{2}\,\xi\big\rangle_A\big|x = -\xi\big\rangle_B$. Further, it is also expressed as

$$\int \mathrm{d}\xi\,\psi(\xi)\big|x = -\sqrt{2}\,\xi\big\rangle_A\big|x = -\xi\big\rangle_B$$
$$\propto \int \mathrm{d}t\,\left|p + \tfrac{1}{\sqrt{2}}f'\left(-\tfrac{x}{\sqrt{2}}\right) = t\right\rangle_A \hat{Z}_B(-\sqrt{2}\,t) \otimes \left(\hat{F}_B^2 \exp\left[-\tfrac{i}{\hbar}f(\hat{x}_B)\right]|\psi\rangle_B\right), \quad \text{(S42)}$$

where $f(x)$ is the arbitrary function of x and $\hat{F} = \hat{R}(\pi/2)$ is the Fourier transform operator. In the same way, by measuring $p + f'(-x/\sqrt{2})/\sqrt{2}$ on mode A, giving measurement results t, and performing the displacement operation $\hat{Z}_B(\sqrt{2}\,t)$, the output state becomes $\hat{F}_B^2 \exp\left[-\tfrac{i}{\hbar}f(\hat{x}_B)\right]|\psi\rangle_B$. When $f(x)$ is higher than a quadratic polynomial, it is a non-Gaussian operation. Note that since it can be accomplished by only using displacement feedforwards, input coupling beam-splitters can also be exchanged. Therefore, by using the extended EPR state, non-Gaussian operations can be performed sequentially, resulting in a resource for universal one-mode universal MBQC.

S3   Data Analysis

S3.1   Influence of Experimental Losses

Experimental imperfections lead to degraded resource squeezing levels. In particular, the unbalanced losses between the optical fiber and free space channels cause the degradation of nullifier variances. Taking into account these losses, instead of equation (S20) we get more involved

theoretical values given by:

$$\left\langle \hat{X}_k^2 \right\rangle = \tfrac{1}{4}\left(\eta^A + \eta_F^A\right)^2 (Sq_A - 1) + \tfrac{1}{4}\left(\eta^B - \eta_F^B\right)^2 (ASq_B - 1) + 1,$$
$$\left\langle \hat{P}_k^2 \right\rangle = \tfrac{1}{4}\left(\eta^B + \eta_F^B\right)^2 (Sq_B - 1) + \tfrac{1}{4}\left(\eta^A - \eta_F^A\right)^2 (ASq_A - 1) + 1, \tag{S43}$$

where Sq_Γ and ASq_Γ are squeezing and anti-squeezing terms for beam $\Gamma(= A, B)$, and η_Γ^2 and $(\eta_\Gamma^F)^2$ are the effective efficiencies of squeezing levels for beam Γ through the free space and optical fiber channels, respectively. To be more precise, η is given by: (quantum efficiency at homodyne detector) $\times$ (influence of intracavity loss $T/(T + L)$) $\times$ (visibility between probe and LO beams)^2 $\times$ (propagation efficiency), where T is the transmittance of the output coupler and L is the intracavity loss in the OPO. In the experiment, these efficiencies are $\eta_A^2 = 88.2\%$, $\eta_B^2 = 89.9\%$, $(\eta_A^F)^2 = 73.7\%$ and $(\eta_B^F)^2 = 75.3\%$. Squeezing levels are calculated as

$$Sq = \int |f(\omega)|^2\, R_-(\omega)\mathrm{d}\omega, \quad ASq = \int |f(\omega)|^2\, R_+(\omega)\mathrm{d}\omega, \tag{S44}$$

$$R_\pm(\omega) = 1 \pm (1 - \eta(\omega))\frac{4x}{(1 \mp x)^2 + (\omega/\gamma)^2}, \tag{S45}$$

where $f(\omega)$ is the Fourier transformation of mode function $f(t)$, $\eta(\omega)$ is the ratio of electrical noise to shot noise at angular frequency ω, x is the pump parameter which is related to the classical parametric amplification gain G as $G = (1 - x)^{-2}$, and γ is the angular frequency half width at half maximum of the OPO. By substituting in these experimental values, we get $\left\langle \hat{X}_k^2 \right\rangle = -5.13$ dB and $\left\langle \hat{P}_k^2 \right\rangle = -5.33$ dB. They agree well with experimental results.

Supplementary References

30. Alexander, R. *et al.* Optimising the temporal mode scheme for single qumode Gaussian operations. in preparation.